An Overview of SaT Segmentation Methodology and Its Applications in Image Processing

Xiaohao Cai, Raymond Chan, and Tieyong Zeng

Abstract As a fundamental and challenging task in many subjects such as image processing and computer vision, image segmentation is of great importance but is constantly challenging to deliver, particularly, when the given images or data are corrupted by different types of degradations like noise, information loss and/or blur. In this article we introduce a segmentation methodology – smoothing and thresholding (SaT) – which can provide a flexible way of producing superior segmentation results with fast and reliable numerical implementations. A bunch of methods based on this methodology are to be presented, including many applications with different types of degraded images in image processing.

Introduction

Image segmentation aims to group objects in an image with similar characteristics together. It is one of the fundamental tasks in image processing and computer vision, having numerous engineering, medical and commercial applications. It also serves as a preliminary step for higher level computer vision tasks like object recognition and interpretation. Most of the methods in literature face the following dilemmas: i) lack of flexibility, applicability and interpretability; and ii) difficult to tradeoff the efficiency and effectiveness. It is therefore not an easy task for users to know which

Xiaohao Cai
School of Electronics and Computer Science, University of Southampton, University Road, Southampton, SO17 1BJ. e-mail: x.cai@soton.ac.uk

Raymond Chan
Department of Mathematics, College of Science, City University of Hong Kong. e-mail: rchan.sci@cityu.edu.hk

Tieyong Zeng
Department of Mathematics, The Chinese University of Hong Kong, Shatin, Hong Kong. e-mail: zeng@math.cuhk.edu.hk

method could fulfil their needs. In this regard, the users are required to make modifications here and there on existing methods accordingly, which is however frustrating if the users are not familiar with segmentation technologies. It is important to have a segmentation methodology which is simple to understand and apply, and at the same time, fast and reliable. In this article, we introduce a segmentation methodology – smoothing and thresholding (SaT) – which is able to meet these challenges Cai et al (2017, 2019, 2013b); Cai and Steidl (2013); Chan et al (2014).

The piecewise constant Mumford-Shah (PCMS) model (nonconvex, a special case of the Mumford-Shah model Mumford and Shah (1989)) and the Rudin-Osher-Fatemi (ROF) model (convex, Rudin et al (1992)) are two of the most famous variational models in the research areas of image segmentation and restoration, respectively. Note that image restoration intends to remove image degradations such as noise, blur or occlusions.

Let $\Omega \subset \mathbb{R}^2$ be a bounded, open set with Lipschitz boundary, and $f : \Omega \to [0,1]$ be a given (degraded) image. In 1989 Mumford and Shah Mumford and Shah (1989) proposed solving segmentation problems by minimizing over $\Gamma \subset \Omega$ and $u \in H^1(\Omega \backslash \Gamma)$ the energy functional

$$E_{\mathrm{MS}}(u,\Gamma;\Omega) = \mathscr{H}^1(\Gamma) + \lambda' \int_{\Omega\backslash\Gamma} |\nabla u|^2 dx + \lambda \int_{\Omega} (u-f)^2 dx, \quad \lambda', \lambda > 0, \quad (1)$$

where $\mathscr{H}^1$ denotes the one-dimensional Hausdorff measure in $\mathbb{R}^2$. The functional E_{MS} contains three terms: the penalty term on the length of Γ, the H^1 semi-norm that enforces the smoothness of u in $\Omega\backslash\Gamma$, and the data fidelity term controlling the distance of u to the given image f. Related approaches in a spatially discrete setting were proposed in Blake and Zisserman (1987); Geman and Geman (1984). An early attempt to solve the challenging task of finding a minimizer of the non-convex and non-smooth Mumford-Shah functional (1) was done by approximating it using a sequence of simpler elliptic problems, see Ambrosio and Tortorelli (1990) for the so-called Ambrosio-Tortorelli approximation. Many approaches to simplify model (1) were meanwhile proposed in the literature, for example, in Pock et al (2009b), a convex relaxation of the model was suggested. Another important simplification is to restrict its solution to be piecewise constant, which leads to the so-called PCMS model.

The PCMS model is based on the restriction $\nabla u = 0$ on $\Omega\backslash\Gamma$, which results in

$$E_{\mathrm{PCMS}}(u,\Gamma;\Omega) = \mathscr{H}^1(\Gamma) + \lambda \int_{\Omega} (u-f)^2 dx. \quad (2)$$

Assuming that $\Omega = \bigcup_{i=0}^{K-1} \Omega_i$ with pairwise disjoint sets Ω_i and constant functions $u(x) \equiv m_i$ on Ω_i, $i = 0, \ldots K-1$, model (2) can be rewritten as

$$E_{\mathrm{PCMS}}(\Omega,m) = \frac{1}{2} \sum_{i=0}^{K-1} \mathrm{Per}(\Omega_i;\Omega) + \lambda \sum_{i=0}^{K-1} \int_{\Omega_i} (m_i - f)^2 dx, \quad (3)$$

where $\Omega := \{\Omega_i\}_{i=0}^{K-1}$, $m := \{m_i\}_{i=0}^{K-1}$, and $\mathrm{Per}(\Omega_i;\Omega)$ denotes the perimeter of Ω_i in Ω. If the number of phases is two, i.e. $K = 2$, the PCMS model is the model of the active contours without edges (Chan-Vese model) Chan and Vese (2001a),

$$E_{\mathrm{CV}}(\Omega_1, m_0, m_1) = \mathrm{Per}(\Omega_1;\Omega) + \lambda\Big(\int_{\Omega_1}(m_1 - f)^2\,dx + \int_{\Omega\setminus\Omega_1}(m_0 - f)^2\,dx\Big). \quad (4)$$

In Chan and Vese (2001a) the authors proposed to solve (4), where it can easily get stuck in local minima. To overcome this drawback, a convex relaxation approach was proposed in Chan et al (2006a). More precisely, it was shown that a global minimizer of $E_{\mathrm{CV}}(\cdot, m_0, m_1)$ for fixed m_0, m_1 can be found by solving

$$\bar{u} = \operatorname*{argmin}_{u\in BV(\Omega)}\Big\{TV(u) + \lambda\int_\Omega \big((m_0 - f)^2 - (m_1 - f)^2\big)u\,dx\Big\}, \quad (5)$$

and setting $\Omega_1 := \{x \in \Omega : \bar{u}(x) > \rho\}$ for any choice of $\rho \in [0,1)$, see also Bellettini et al (1991); Bresson et al (2007). Note that the first term of (5) is known as the total variation (TV) and the space BV is the space of functions of bounded variation, see Section 2 for the definition. In other words, (5) is a tight relaxation of the Chan-Vese model with fixed m_0 and m_1. For the convex formulation of the full model (4), see Brown et al (2012).

There are many other approaches for two-phase image segmentation based on the Chan-Vese model and its convex version, see e.g. Zhang et al (2008); Bresson et al (2007); Dong et al (2010); Bauer et al (2017). In particular, a hybrid level set method was proposed in Zhang et al (2008), which replaces the first term of (4) by a boundary feature map and the data fidelity terms in (4) by the difference between the given image f and a fixed threshold chosen by a user or a specialist. Method Zhang et al (2008) was used in medical image segmentation. However, since every time it needs the user to choose a proper threshold for its model, it is not automatic and thus its applications are restricted. In Bresson et al (2007), the TV term of (5) was replaced by a weighted TV term which helps the new model to capture much more important geometric properties. In Dong et al (2010), the TV term of (5) was replaced by a wavelet frame decomposition operator which, similar to the model in Bresson et al (2007), can also capture important geometric properties. Nevertheless, for its solution u, no similar conclusions as the ones in Chan et al (2006a) can be addressed; that is, there is no theory to support that its segmentation result $\Omega_1 = \{x : u(x) > \rho\}$ for $\rho \in [0,1)$ is a solution as to some kind of objective functional. In Bauer et al (2017), the Chan-Vese model was extended for 3D biopores segmentation in tomographic images.

In Vese and Chan (2002), Chan and Vese proposed a multiphase segmentation model based on the PCMS model using level sets. However, this method can also get stuck easily in local minima. Convex (non-tight) relaxation approaches for the PCMS model were proposed, which are basically focusing on solving

$$\min_{m_i,u_i\in[0,1]}\Big\{\sum_{i=0}^{K-1}\int_\Omega |\nabla u_i|dx + \lambda\sum_{i=0}^{K-1}\int_\Omega (m_i - f)^2 u_i dx\Big\}, \quad \text{s.t.} \sum_{i=0}^{K-1} u_i = 1. \quad (6)$$

For more details along this line, refer e.g. to Bar et al (2011); Cai (2015); Cai et al (2015); Lellmann and Schnörr (2011); Li et al (2010); Pock et al (2009a); Yuan et al (2010b); Zach et al (2008) and the references therein.

In 1992, Rudin, Osher and Fatemi Rudin et al (1992) proposed the variational model

$$\min_{u\in BV(\Omega)} \left\{ TV(u) + \frac{\mu}{2}\int_{\Omega} \left(u-f\right)^2 dx \right\}, \quad \mu > 0. \tag{7}$$

which has been studied extensively in the literature, see e.g. Chambolle (2005); Chambolle et al (2010); Chan et al (2006b) and references therein.

A subtle connection between image segmentation and image restoration has been raised in Cai et al (2013b). In detail, a two-stage image segmentation method is proposed – SaT method – which finds the solution of a convex variant of the Mumford-Shah model in the first stage followed by a thresholding step in the second one. The convex minimization functional in the first stage (the smoothing stage) is the ROF functional (7) plus an additional smoothing term $\int_{\Omega} |\nabla u|^2 \, dx$. In Cai et al (2019), a linkage between the PCMS and ROF models was shown, which gives rise to a new image segmentation paradigm: manipulating image segmentation through image restoration plus thresholding. This is also the essence of the SaT segmentation methodology.

The remainder of this article is organised as follows. Firstly, the SaT segmentation and its advantages are introduced. After that, more SaT-based methods and applications are presented and demonstrated, followed by a brief conclusion.

SaT Methodology

The main procedures of the SaT segmentation methodology are first smoothing and then thresholding, where the smoothing step is executed by solving pertinent convex objective functions (note that most of segmentation models in literature are non-convex and therefore much harder to handle compared to convex models) and the thresholding step is just completed by thresholding the result from the smoothing step using proper thresholds, see an instance given below.

The smoothing process in Cai et al (2013b) is to solve the convex minimization problem (cf. the non-smooth Mumford-Shah functional (1))

$$\inf_{g\in W^{1,2}(\Omega)} \left\{ \frac{\mu}{2}\int_{\Omega} (f-Ag)^2 \mathrm{d}x + \frac{\lambda}{2}\int_{\Omega} |\nabla g|^2 \mathrm{d}x + \int_{\Omega} |\nabla g| \mathrm{d}x \right\}, \tag{8}$$

where λ and μ are positive parameters, and A is the blurring operator if the observed image is blurred by A or the identity operator if there is no blurring. The minimizer of (8) is a smoothed approximation of f. The first term in (8) is the data-fitting term, the second term ensures smoothness of the minimizer, and the third term ensures regularity of the level sets of the minimizer. We emphasize that model (8) can be minimized quickly by using currently available efficient algorithms such as the split-

Bregman algorithm Goldstein and Osher (2009) or the Chambolle-Pock method Chambolle and Pock (2011). After we have obtained g in (8), assume we are given the thresholds

$$\min\{g\} = \rho_0 < \rho_1 < \cdots < \rho_{K-1} < \rho_K = \max\{g\}.$$

Then we threshold g by setting $x \in \Omega$ to be in the sub-domain Ω_i if $\rho_{i-1} \leq g(x) < \rho_i$. The values $\{\rho_i\}_{i=1}^{K-1}$ can be obtained by applying the K-means method, a popular clustering method, on the intensity of g, or they can be obtained by trial and error in order to get a finer segmentation.

Theorem 1. *Let Ω be a bounded connected open subset of $\mathbb{R}^2$ with a Lipschitz boundary. Let $f \in L^2(\Omega)$ and $\mathrm{Ker}(A) \bigcap \mathrm{Ker}(\nabla) = \{0\}$, where A is a bounded linear operator from $L^2(\Omega)$ to itself and $\mathrm{Ker}(A)$ is the kernel of A. Then (8) has a unique minimizer $g \in W^{1,2}(\Omega)$.*

Proof. See Cai et al (2013b) for the detailed proof.

Figures 1, 2 and 3 illustrate the SaT framework using the two-phase segmentation strategy in Cai et al (2013b).

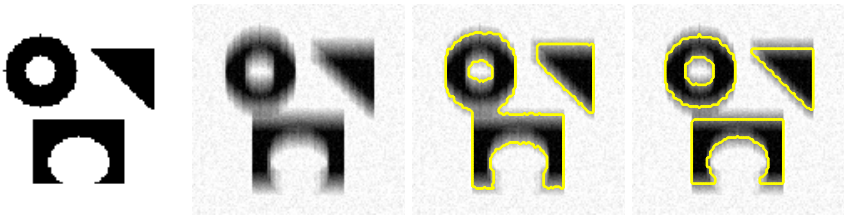

(a) given image (b) degraded image (c) Chan-Vese method (d) Cai et al (2013b)

Fig. 1 Segmentations with Gaussian noise and blur. (a): Given binary image; (b): degraded image with motion blur (for the motion blur, the motion is vertical and the filter size is 15) and Gaussian noise (with mean 10^{-3} and variance 2×10^{-3}); (c): Chan-Vese method Chan and Vese (2001b); and (d): SaT segmentation with K-means thresholding Cai et al (2013b).

The good performance of the SaT approach is solidly backed up. If we set the parameter λ in (8) to zero, one can show (see Cai and Steidl (2013); Cai et al (2019)) that the SaT method is equivalent to the famous Chan-Vese segmentation method (Chan and Vese (2001b)), which is a simplified Mumford-Shah model. Furthermore, numerical experiments show that a properly selected λ can usually increase segmentation accuracies.

The SaT method is very efficient and flexible. It performs excellently for degraded images (e.g. noisy and blurry images and images with information loss). It also has the following advantages. Firstly, the smoothing model with (8) is strictly convex. This guarantees a unique solution of (8), which can be solved efficiently by many optimization methods. Secondly, the thresholding step is independent of

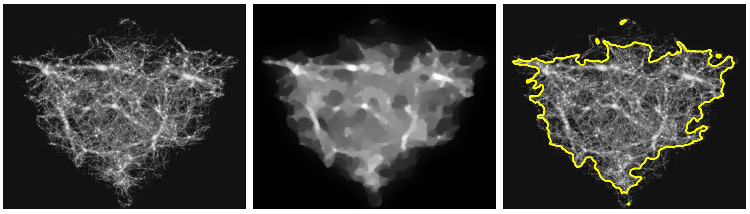

(a) given image (b) smoothing (c) thresholding

Fig. 2 SaT segmentation framework illustration using a two-phase segmentation example. (a): given image (size 384×480); (b): obtained smoothed image (i.e. a solution of the convex model in Cai et al (2013b)); (c): segmentation result (boundary highlighted in yellow color) after thresholding (b) using threshold 0.2. Particularly, (b) and (c) correspond to the first and second steps in the SaT segmentation framework, respectively.

the smoothing step. Therefore the SaT approach is capable of segmentations with arbitrary phases, and one can easily try different thresholds without recalculating (8). On the contrary, for other segmentation methods, the number of phases K has to be determined before the calculation and it is usually computationally expensive to re-generate a different segmentation if K changes. Thirdly, the SaT approach is very flexible. One can easily modify the smoothing step to better segment images with specific properties.

The SaT segmentation methodology has been used for images corrupted by Poisson and Gamma noises Chan et al (2014), degraded color images Cai et al (2017), images with intensity inhomogeneity Chan et al (2019), hyperspectral images Chan et al (2020), vascular structures Cai et al (2011, 2013a), spherical images Cai et al (2020), etc.

SaT-based Methods and Applications

To exemplify the excellent performance of the SaT segmentation methodology, in the following a few methods related to the SaT segmentation methodology with different applications are introduced.

T-ROF method

In Cai and Steidl (2013); Cai et al (2019), the *thresholded-ROF* (T-ROF) method was proposed. It highlights a relationship between the PCMS model (3) and the ROF model (7), proving that thresholding the minimizer of the ROF model leads to a partial minimizer of the PCMS model when $K = 2$ (Chan-Vese model (4)), which remains true under specific assumptions when $K > 2$.

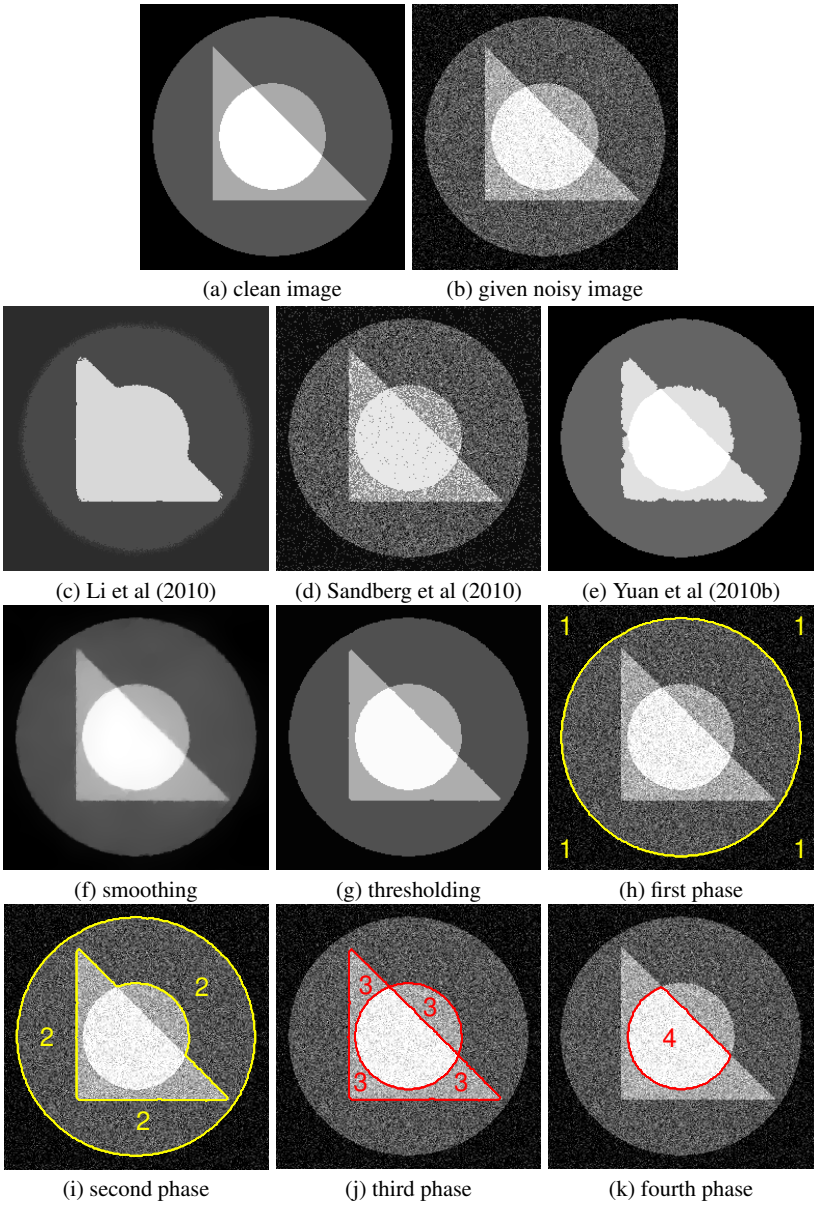

(a) clean image (b) given noisy image

(c) Li et al (2010) (d) Sandberg et al (2010) (e) Yuan et al (2010b)

(f) smoothing (g) thresholding (h) first phase

(i) second phase (j) third phase (k) fourth phase

Fig. 3 Four-phase segmentation. (a): clean 256×256 image; (b): given noisy image (Gaussian noise with zero mean and variance 0.03); (c)–(e): results of methods Li et al (2010), Sandberg et al (2010) and Yuan et al (2010b) respectively; (f): obtained smoothed image (i.e. a solution of the convex model in Cai et al (2013b)); (g): segmentation result after thresholding (f) using thresholds $\rho_1 = 0.1652, \rho_2 = 0.4978, \rho_3 = 0.8319$; (h)–(k) boundary of each phase of the result in (g).

Theorem 2. (Relation between ROF and PCMS models for $K = 2$) *Let $K = 2$ and $u^* \in BV(\Omega)$ solve the ROF model* (7)*. For given $0 < m_0 < m_1 \leq 1$, let $\tilde{\Sigma} := \{x \in \Omega : u^*(x) > \frac{m_1+m_0}{2}\}$ fulfill $0 < |\tilde{\Sigma}| < |\Omega|$. Then $\tilde{\Sigma}$ is a minimizer of the PCMS model* (4) *for $\lambda := \frac{\mu}{2(m_1-m_0)}$ and fixed m_0, m_1. In particular, $(\tilde{\Sigma}, m_0, m_1)$ is a partial minimizer of* (4) *if $m_0 = \text{mean}_f(\Omega \backslash \tilde{\Sigma})$ and $m_1 = \text{mean}_f(\tilde{\Sigma})$.*

Proof. See Cai et al (2019) for the detailed proof.

This linkage between the PCMS model and the ROF model validates the effectiveness of the proposed SaT method in Cai et al (2013b) for image segmentation. Due to the significance of the PCMS model and ROF model, respectively in image segmentation and image restoration, this linkage bridges to some extent these two research areas and might serve as a motivation to improve and design better methods. A direct benefit is the newly proposed efficient segmentation method – T-ROF method. The T-ROF method exactly follows the paradigm to perform image segmentation through image restoration plus iterative thresholding, where these thresholds are selected automatically following certain rules. This appears to be more sophisticated than the SaT method Cai et al (2013b) which is based on K-means. It is worth emphasizing that the ROF model and the T-ROF model both need to be solved once, and the T-ROF method gives optimal segmentation results akin to the PCMS model. The convergence of the T-ROF method regarding thresholds automatic selection is also proved.

On the one hand, the T-ROF method can be regarded as a special case of the SaT method. However, it is directly obtained from the linkage between the PCMS model and the ROF model and thus is more theoretically justified. Moreover, the strategy of choosing the thresholds automatically and optimally in the T-ROF method is not covered in the SaT method in Cai et al (2013b). The strategy makes the T-ROF method more effective particularly for degraded images whose phases have close intensities. On the other hand, the T-ROF method inherits the advantages of the SaT method – fast speed and computational cost independent of the required number of phases K. In contrast, methods solving the PCMS model become computational demanding as the required number of phases increases.

To demonstrate the great performance of the T-ROF method, Figure 4 gives an example of segmenting a synthetic retina image based on one manually segmented result from the DRIVE data-set[1]. Fig. 4 (a) and (b) are the clean manual segmentation image and the noisy image generated by adding Gaussian noise with mean 0 and variance 0.1. Note that in Fig. 4 (a), the original binary manual segmentation image is changed to three phases by lowering the intensity of those vessels on the right hand side from 1 to 0.3; the intensities of the background and the vessels on the left hand side are respectively 0 and 1. Obviously, segmenting the noisy three-phase image in Fig. 4 (b) is extremely challenging due to those thin blood vessels which have a big chance of being smoothed out. Figure 4 shows that the T-ROF method together with the SaT method Cai et al (2013b) achieve the best result (with much

[1] http://www.isi.uu.nl/Research/Databases/DRIVE/

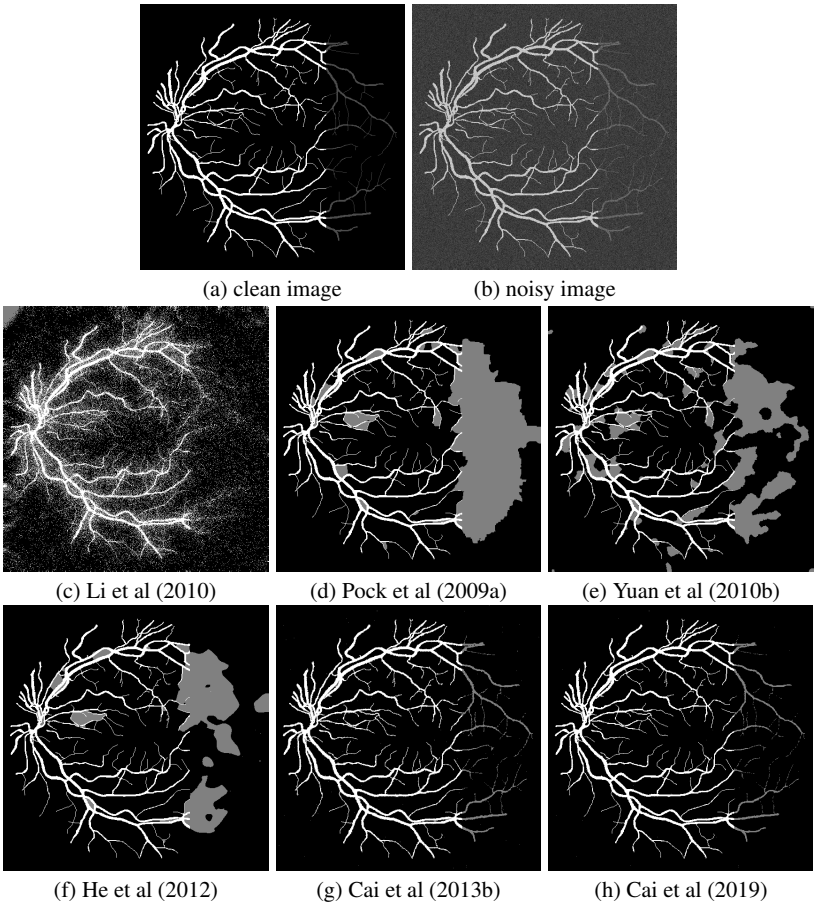

(a) clean image (b) noisy image

(c) Li et al (2010) (d) Pock et al (2009a) (e) Yuan et al (2010b)

(f) He et al (2012) (g) Cai et al (2013b) (h) Cai et al (2019)

Fig. 4 Retina image segmentation which contains extremely thin vessels (size 584×565). (a): Clean image; (b): noisy image; (c)–(h): results of methods Li et al (2010); Pock et al (2009a); Yuan et al (2010b); He et al (2012); Cai et al (2013b) and the T-ROF method Cai et al (2019), respectively.

faster speed compared with others). For more details of the T-ROF method please refer to Cai and Steidl (2013); Cai et al (2019).

Two-stage method for Poisson or Gamma noise

The Poisson noise and the multiplicative Gamma noise are firstly recalled below. For the Poisson noise, for each pixel $x \in \Omega$ we assume that the intensity $f(x)$ is a random variable following the Poisson distribution with mean $g(x)$, i.e., its probability mass

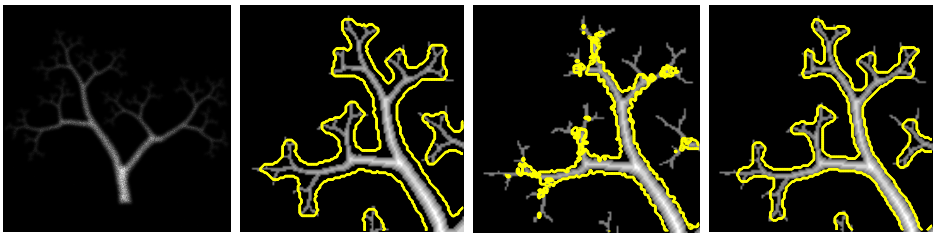

(a) given image (b) (c) (d)

Fig. 5 Segmentations of a fractal image corrupted with Gamma noise and blur. (a): Degraded image; (b)–(d): results of methods Yuan et al (2010a), Dong et al (2011), and SaT with user-provided thresholds Chan et al (2014), respectively. For clarity, only the top-left corner of the segmentations are shown. We see that the SaT method produces the best result, with the segmentation line (the yellow line) very close to the real boundary.

function is:

$$p_{f(x)}(n;g(x)) = \frac{(g(x))^n e^{-g(x)}}{n!},$$

where n is the intensity of f at the pixel x. In this case, we say that f is corrupted by Poisson noise. For the Gamma noise, suppose that for each pixel $x \in \Omega$ the random variable $\eta(x)$ follows the Gamma distribution, i.e., its probability density function is:

$$p_{\eta(x)}(y;\theta,K) = \frac{1}{\theta^K \Gamma(K)} y^{K-1} e^{-\frac{y}{\theta}} \text{ for } y \geq 0, \tag{9}$$

where Γ is the usual Gamma-function, θ and K denote the scale and shape parameters in the Gamma distribution respectively. Notice that, the mean of $\eta(x)$ is $K\theta$, and the variance of $\eta(x)$ is $K\theta^2$. For multiplicative noise, we assume in general that the mean of $\eta(x)$ equals 1, see Aubert and Aujol (2008); Durand et al (2010). Then we have $K\theta = 1$ and its variance is $1/K$. We assume the degraded image is $f(x) = g(x) \cdot \eta(x)$, and say that f is corrupted by multiplicative Gamma noise.

The construction of a data-fidelity term can be inspired by the following observations. With the abuse of notation, suppose f is the given image with noise following a certain statistical distribution, and let $p(g|f)$ be the conditional probability of g when we have observed f. Then based on maximum-a-posteriori approach, restoring the image g is equivalent to maximizing the probability $p(g|f)$. Assume the prior distribution of g is given by

$$p(g) \propto \exp\left(-\beta \int_\Omega |\nabla g| dx\right),$$

where β is a parameter. If the noise follows the Poisson distribution, then maximizing $p(g|f)$ corresponds to minimizing the functional

$$\int_\Omega (g - f \log g) dx + \beta \int_\Omega |\nabla g| dx, \tag{10}$$

see T. Le and Asaki (2007). If the noise is multiplicative following the Gamma distribution, then maximizing $p(u|f)$ corresponds to minimizing the functional

$$\int_\Omega (\frac{f}{g} + \log g)dx + \beta \int_\Omega |\nabla g|dx, \tag{11}$$

see Aubert and Aujol (2008). However, it is observed in the numerical examples in Aubert and Aujol (2008); Shi and Osher (2008) that for the denoising model (11) the noise survives much longer at low image values if we increase the regularization parameter. Therefore, in Shi and Osher (2008) the authors suggested to take $w = \log g$ and change the objective functional (11) to

$$\int_\Omega (fe^{-w} + w)dx + \beta \int_\Omega |\nabla w|dx. \tag{12}$$

In Chan et al (2014), a two-stage method for segmenting blurry images in the presence of Poisson or multiplicative Gamma noise is proposed. It was inspired by the SaT segmentation method in Cai et al (2013b) and the Gamma noise denoising method in Steidl and Teuber (2010). Specifically, the data fidelity term of the model (8) at the first stage of the SaT segmentation method in Cai et al (2013b) was replaced by the one which is suitable for Gamma noise, i.e.,

$$\inf_{g\in W^{1,2}(\Omega)} \left\{ \mu \int_\Omega (Ag - f\log Ag)dx + \frac{\lambda}{2}\int_\Omega |\nabla g|^2 \mathrm{d}x + \int_\Omega |\nabla g| \mathrm{d}x \right\}. \tag{13}$$

Then at the second stage the solution g is thresholded to reveal different segmentation features.

The follow Theorems 3 and 4 assure that model (13) has a unique minimizer with identity or blurring operator A.

Theorem 3. *Let Ω be a bounded connected open subset of $\mathbb{R}^2$ with a Lipschitz boundary. Let $f \in L^\infty(\Omega)$ with $\inf f > 0$ and A be the identity operator. Then (13) has a unique minimizer $u \in W^{1,2}(\Omega)$ satisfying $0 < \inf f \le u \le \sup f$.*

Proof. See Chan et al (2014) for the detailed proof.

Theorem 4. *Let Ω be a bounded connected open subset of $\mathbb{R}^2$ with a Lipschitz boundary. Let $f \in L^\infty(\Omega)$ with $\inf f > 0$, and let $\mathscr{A}$ be a continuous linear operator from $W^{1,2}(\Omega)$ to itself. Assume $Ker(\mathscr{A}) \cap Ker(\nabla) = \{0\}$, then (13) has a unique minimizer $u \in W^{1,2}(\Omega)$.*

Proof. See Chan et al (2014) for the detailed proof.

Figure 5 gives an example which shows the great performance of the SaT based method Chan et al (2014) for images with multiplicative Gamma noise.

SLaT method for color images

Extending or conceiving segmentation methods for color images is not a simple task since one needs to discriminate segments with respect to both luminance and chrominance information. The two-phase Chan-Vese model Chan and Vese (2001a) was generalized to deal with vector-valued images in Chan et al (2000) by combining the information in the different channels using the data fidelity term. Many methods are applied in the usual RGB color space Cai (2015); Chan et al (2000); Cremers et al (2007a); Jung et al (2007); Kay et al (2009); Martin et al (2001); Pock et al (2009a); Storath and Weinmann (2014), among others. It is often mentioned that the RGB color space is not well adapted to segmentation because for real-world images the R, G and B channels can be highly correlated. In Rotaru et al (2008), RGB images are transformed into HSI (hue, saturation, and intensity) color space in order to perform segmentation. In Benninghoff and Garcke (2014) a general segmentation approach was developed for gray-value images and further extended to color images in the RGB, the HSV (hue, saturation, and value) and the CB (chromaticity-brightness) color spaces. However, a study on this point in Paschos (2001) has shown that the Lab (perceived lightness, red-green and yellow-blue) color space defined by the CIE (Commission Internationale de l'Eclairage) is better adapted for color image segmentation than the RGB and the HSI color spaces. In Cardelino et al (2013) RGB input images were first converted to Lab space. In Wang et al (2015) color features were described using the Lab color space and texture using histograms in RGB space.

A careful examination of the methods that transform a given RGB image to another color space (HSI, CB, Lab, etc.) before performing the segmentation task has shown that these algorithms are always applied only to noise-free RGB images (though these images unavoidably contain quantization and compression noise). For instance, this is the case of Benninghoff and Garcke (2014); Cardelino et al (2013); Rotaru et al (2008); Wang et al (2015), among others. One of the main reasons is that if the input RGB image is degraded, the degradation would be hard to control after a transformation to another color space Paschos (2001).

A color image is usually represented by a vector valued function $f = (f_1, f_2, f_3) : \Omega \to \mathbb{R}^3$, where the components f_1, f_2 and f_3 generally represent red, green and blue channels respectively. The difficulty for color image segmentation partly comes from the strong inter-channel correlation. A novel extension of the SaT approach is the smoothing, lifting and thresholding (SLaT) method introduced in Cai et al (2017), which is able to work on vector-valued (color) images possibly corrupted with noise, blur and missing data. One first solves (8) for the three components f_1, f_2 and f_3 to obtain three smooth functions g_1, g_2 and g_3. Then one transforms (g_1, g_2, g_3) to another color space $(\bar{g}_1, \bar{g}_2, \bar{g}_3)$ which can reduce inter-channel correlation. This is the lifting process, and the Lab color space is usually a good choice. In the thresholding step one performs K-means to threshold the lifted image with 6 channels $(g_1, g_2, g_3, \bar{g}_1, \bar{g}_2, \bar{g}_3)$ to get the phases.

In Cai et al (2017), model (8) was also extended to tackle information loss and both Gaussian and Poisson noise. In particular, the existence and uniqueness of the

extended model with information loss and both Gaussian and Poisson noise was also proved.

This SLaT method is easy to implement with promising results, see Figure 6 with images chosen from the Berkeley Segmentation Dataset and Benchmark[2]. Moreover, the SLaT method has the ability to segment color images corrupted by noise, blur, or when some pixel information is lost. More experimental results in Cai et al (2017) on RGB images coupled with Lab secondary color space demonstrate that the method gives much better segmentation results for images with degradation than some state-of-the-art segmentation models both in terms of quality and CPU time cost.

Fig. 6 Color image segmentation for degraded images. First row: degraded color images (the first three images are degraded by various noise and blur, and the last two images are degraded by 60% information loss and noise). Second row: Pock et al (2009a). Third row: SLaT method Cai et al (2017).

Two-stage method for hyperspectral images

Remotely sensed hyperspectral images are images taken from drones, airplanes or satellites that record a wide range of electromagnetic spectrum, typically more than 100 spectral bands from visible to near-infrared wavelengths. Since different materials reflect different spectral signatures, one can identify the materials at each pixel of the image by examining its spectral signatures. Hyperspectral images are used in many applications, including agriculture Patel et al (2001); Datt et al (2003), disaster relief Eismann et al (2009), food safety Gowen et al (2007), military Manolakis and Shaw (2002); Stein et al (2002) and mineralogy Hörig et al (2001).

[2] https://www2.eecs.berkeley.edu/Research/Projects/CS/vision/bsds/

One of the most important problems in hyperspectral data exploitation is hyperspectral images classification. It has been an active research topic in past decades Fauvel et al (2013). The pixels in the hyperspectral image are often labeled manually by experts based on careful review of the spectral signatures and investigation of the scene. Given these ground-truth labels of some pixels (also called "training pixels"), the objective of hyperspectral images classification is to assign labels to part or all of the remaining pixels (the "testing pixels") based on their spectral signatures and their locations.

In Chan et al (2020), a two-stage method was proposed based on the SaT method Cai et al (2013b) for hyperspectral images classification. Pixel-wise classifiers, such as the classical support vector machine (SVM), consider spectral information only. As spatial information is not utilized, the classification results are not optimal and the classified image may appear noisy. Many existing methods, such as morphological profiles, superpixel segmentation, and composite kernels, exploit the spatial information. In Chan et al (2020), a two-stage approach was proposed. In the first stage, SVMs are used to estimate the class probability for each pixel. In the second stage, the SaT model is applied to each probability map to denoise and segment the image into different classes. The proposed method effectively utilizes both spectral and spatial information of the data sets and is fast as only convex minimization is needed in addition to the SVMs.

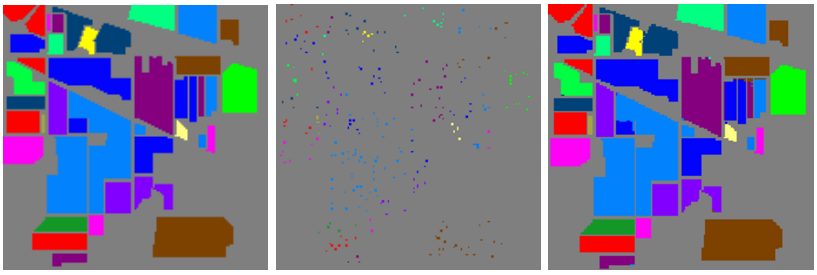

(a) ground truth (b) training set (c) Chan et al (2020)

Fig. 7 Hyperspectral image classification of the Indian Pines data set. (a) Ground truth, (b) training set (10% of total pixels), and (c) classification with SaT Chan et al (2020) (98.83% overall accuracy).

We emphasize that the convex model used in Chan et al (2020) is the model (8) at the first stage of the SaT segmentation method in Cai et al (2013b), with a constraint, i.e.,

$$\begin{aligned} &\inf_{g_k}\left\{\frac{\mu}{2}\int_\Omega (f_k - Ag_k)^2 \mathrm{d}x + \frac{\lambda}{2}\int_\Omega |\nabla g_k|^2 \mathrm{d}x + \int_\Omega |\nabla g_k| \mathrm{d}x\right\}, \\ &\text{s.t. } g_k|_{\Omega_{\text{train}}} = f_k|_{\Omega_{\text{train}}}, \end{aligned} \tag{14}$$

where f_k represents the probability map of the k-th class obtained from stage one using the SVM method, g_k is the improved probability map of the k-th class, and Ω_{train} is the set of training pixels. After obtaining $g_k, k = 1\ldots,K$, individual pixels will be labeled to a set which possesses the maximum values among $g_k(x), k = 1\ldots,K$. Note that the above stage two performs like the SaT strategy.

Figure 7 gives an example which shows the great performance of the two-stage method Chan et al (2020) for hyperspectral images classification. More details please refer to Chan et al (2020).

Tight-frame based method for images with vascular structures

The segmentation problem of branching tubular objects in 2D and 3D images arises in many applications, for examples, extracting roads in aerial photography, and anatomical surfaces of blood vessels in medical images. Identifying tube-like structures is of great importance in medical imaging, with the primary application of segmenting blood vessels in magnetic resonance angiography (MRA) images. Unlike classical segmentation problems, vessel segmentation is characterized by different aims such as (a) detect correctly branches and complex topologies, (b) detect vessels of very different thickness (from very thin to very thick), (c) repair small occlusions (false disconnections), (d) remove noise incorrectly segmented, and (e) control the minimum thickness of the vessels by a user given precision. Moreover, when used in a real-time medical environment, automatic, robust and efficient methods are essential. All these requirements make the vessel segmentation problem very challenging.

Many different approaches for image segmentation and, in particular, vessel segmentation have been proposed in literature, see for example Chapman et al (2004); Chen and Amini (2004); Dong et al (2010); Franchini et al (2010); Gooya et al (2008); Krissian et al (2000); Lorigo et al (2001); Sum and Cheung (2008); Yan and Kassim (2006); Zonoobi et al (2009) and the extended reviews Cremers et al (2007b); Kirbas and Quek (2004). Below we give a brief account of some of these methods.

In Cai et al (2011, 2013a), a tight-frame based method was proposed to automatically identify tube-like structures in medical imaging, with the primary application of segmenting blood vessels in magnetic resonance angiography images. The method iteratively refines a region that encloses the potential boundary of the vessels. At each iteration, the tight-frame algorithm was applied to denoise and smooth the potential boundary and sharpen the region, in a similar fashion as the SaT strategy. The cost per iteration is proportional to the number of pixels in the image. It is proved that the iteration converges in a finite number of steps to a binary image whereby the segmentation of the vessels can be done straightforwardly.

Let $\mathbf{f} = \text{vec}(f)$ denotes the vector obtained by concatenating the columns of f. It is worth mentioning the tight-frame algorithms used in e.g. Cai et al (2008) can be presented in the following generic form:

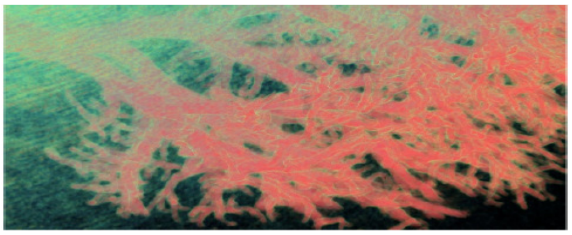

(a) given CTA image

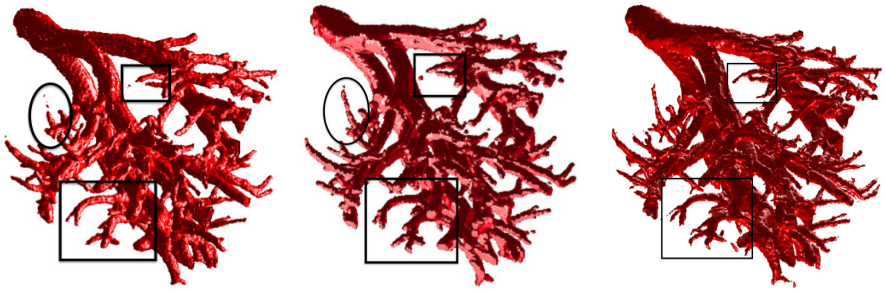

(b) Lorigo et al (2001) (c) Franchini et al (2009) (d) Cai et al (2013a)

Fig. 8 Segmentation of the kidney volume data set. (a): Given CTA image; (b): CURVES segmentation Lorigo et al (2001); (c): ADA segmentation Franchini et al (2009); (d) tight-frame based method Cai et al (2013a).

$$\mathbf{f}^{(i+\frac{1}{2})} = \mathscr{U}(\mathbf{f}^{(i)}), \tag{15}$$

$$\mathbf{f}^{(i+1)} = \mathscr{A}^T \mathscr{T}_\lambda(\mathscr{A}\mathbf{f}^{(i+\frac{1}{2})}), \quad i = 1,2,\ldots. \tag{16}$$

Here $\mathbf{f}^{(i)}$ is an approximate solution at the i-th iteration, $\mathscr{U}$ is a problem-dependent operator, and $\mathscr{T}_\lambda(\cdot)$ is the soft-thresholding operator defined as follows. Given vectors $\mathbf{v} = [v_1,\cdots,v_n]^T$ and $\lambda = [\lambda_1,\cdots,\lambda_n]^T$, $\mathscr{T}_\lambda(\mathbf{v}) \equiv [t_{\lambda_1}(v_1),\cdots,t_{\lambda_n}(v_n)]^T$, where

$$t_{\lambda_k}(v_k) \equiv \begin{cases} \mathrm{sgn}(v_k)(|v_k| - \lambda_k), & \text{if } |v_k| > \lambda_k, \\ 0, & \text{if } |v_k| \le \lambda_k. \end{cases} \tag{17}$$

Let $P^{(i+1)}$ be the diagonal matrix where the diagonal entry is 1 if the corresponding index is in $\Lambda^{(i+1)}$, and 0 otherwise. Then

$$\mathbf{f}^{(i+1)} \equiv (I - P^{(i+1)})\mathbf{f}^{(i+\frac{1}{2})} + P^{(i+1)}\mathscr{A}^T \mathscr{T}_\lambda(\mathscr{A}\mathbf{f}^{(i+\frac{1}{2})}). \tag{18}$$

By reordering the entries of the vector $\mathbf{f}^{(i+1)}$ into columns, we obtain the image $f^{(i+1)}$. We remark that the effect of (18) is to denoise and smooth the image on $\Lambda^{(i+1)}$.

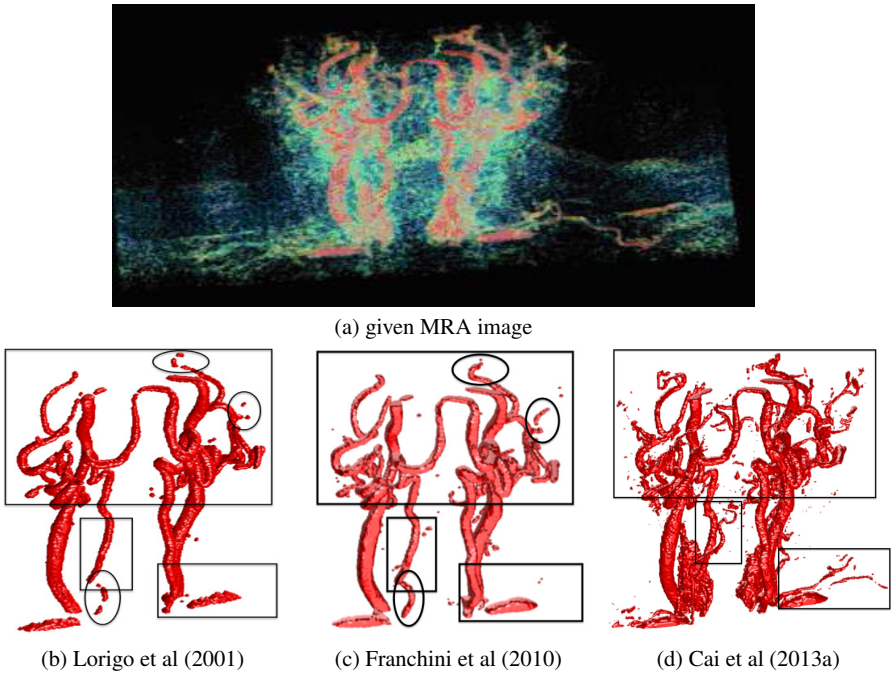

(a) given MRA image

(b) Lorigo et al (2001) (c) Franchini et al (2010) (d) Cai et al (2013a)

Fig. 9 Segmentation of the brain volume data set. (a): Given MRA image; (b): CURVES segmentation Lorigo et al (2001); (c): ADA segmentation Franchini et al (2010); (d) tight-frame based method Cai et al (2013a).

Figures 8 and 9 give examples which show the great performance of the tight-frame based method Cai et al (2013a) for images with tube-like structures. More details please refer to Cai et al (2013a).

Wavelet-based segmentation method for spherical images

Spherical images are common in nature, for example, in cosmology McEwen et al (2007b), astrophysics Schmitt et al (2012), planetary science Audet (2014), geophysics Simons et al (2011), and neuro-science Rathi et al (2011), where images are naturally defined on the sphere. Clearly, images defined on the sphere are different to Euclidean images in 2D and 3D in terms of symmetries, coordinate systems and metrics constructed (see for example Li and Hai (2010)).

Wavelets have become a powerful analysis tool for spherical images, due to their ability to simultaneously extract both spectral and spatial information. A variety of wavelet frameworks have been constructed on the sphere in recent years, e.g. Baldi et al (2009); McEwen et al (2018), and have led to many insightful scientific studies

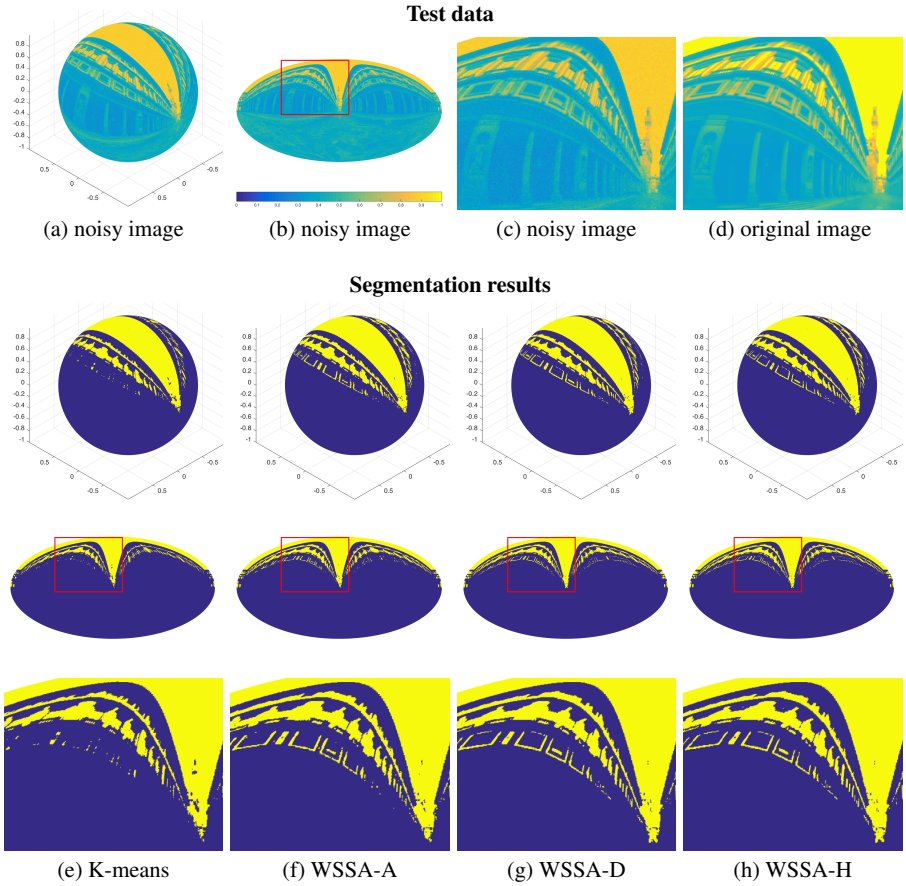

(a) noisy image (b) noisy image (c) noisy image (d) original image

(e) K-means (f) WSSA-A (g) WSSA-D (h) WSSA-H

Fig. 10 Results of light probe image - the Uffizi Gallery. First row: noisy image shown on the sphere (a) and in 2D using a mollweide projection (b), and the zoomed-in red rectangle area of the noisy (c) and original images (d), respectively; Second to fourth rows from left to right: results of methods K-means (e), WSSA-A (f), WSSA-D (g) with $N = 6$ (even N), and WSSA-H (h), respectively. Note that methods WSSA-A, WSSA-D and WSSA-H are the wavelet-based segmentation method Cai et al (2020) respectively equipped with axisymmetric wavelets, directional wavelets and hybrid wavelets defined on the sphere.

in the fields mentioned above (see McEwen et al (2007b); Schmitt et al (2012); Audet (2014); Simons et al (2011); Rathi et al (2011)). Different types of wavelets on the sphere have been designed to probe different structure in spherical images, for example isotropic or directional and geometrical features, such as linear or curvilinear structures, to mention a few. Axisymmetric wavelets Baldi et al (2009); Leistedt et al (2013) are useful for probing spherical images with isotropic structure, directional wavelets McEwen et al (2018) for probing directional structure, ridgelets Michailovich and Rathi (2010); Starck et al (2006) for analysing antipodal signals on the sphere, and curvelets Starck et al (2006); Chan et al (2017) for studying

highly anisotropic image content such as curve-like features (we refer to Candés and Donoho (2005) for the general definition of Euclidean ridgelets and curvelets). Fast algorithms have been developed to compute exact forward and inverse wavelet transforms on the sphere for very large spherical images containing millions of pixels McEwen et al (2007a). Localisation properties of wavelet constructions have also been studied in detail McEwen et al (2018), showing important quasi-exponential localisation and asymptotic uncorrelation properties for certain wavelet constructions. An investigation into the use of axisymmetric and directional wavelets for sparse image reconstruction was performed recently in Wallis et al (2017), showing excellent performance.

In Cai et al (2020), a wavelet-based method was proposed to segment images on the sphere, accounting for the underlying geometry of spherical data. The method is a direct extension of the tight-frame based segmentation method Cai et al (2011, 2013a) used to automatically identify tube-like structures such as blood vessels in medical imaging. It is compatible with any arbitrary type of wavelet frame defined on the sphere, such as axisymmetric wavelets, directional wavelets, curvelets, and hybrid wavelet constructions. Such an approach allows the desirable properties of wavelets to be naturally inherited in the segmentation process. In particular, directional wavelets and curvelets, which were designed to efficiently capture directional signal content, provide additional advantages in segmenting images containing prominent directional and curvilinear features.

Figure 10 gives an example which shows the great performance of the wavelet-based segmentation method for spherical images. More details please refer to Cai et al (2020).

Three-stage method for images with intensity inhomogeneity

The intensity inhomogeneity is a common phenomenon in real-world images and may bring considerable difficulties for image segmentation Li et al (2008). The intensity inhomogeneity can be roughly divided into two types: the extrinsic one and the intrinsic one. The extrinsic intensity inhomogeneity is globally revoked by the image acquisition devices or illumination variations which frequently appear in medical images. On the other hand, the intrinsic one is caused by the local discrepancy of the image color, intensity, or texture pattern in objects and backgrounds which usually appear in natural images.

The extrinsic inhomogeneous intensities are usually smoothly varying. Involving the local intensity information in the energy functional is a common way to address the issue of extrinsic inhomogeneity. Li et al (2008) and Wang et al (2010) used Gaussian kernel methods to characterize the intensities in local regions. The intrinsic intensity inhomogeneity varies sharply. Some texture segmentation algorithms (e.g., Brox et al (2010) and Cremers et al (2007a)) have been proposed to tackle such kinds of intensity inhomogeneity. New features (e.g., structure tensors Ge et al (2015), salient information Kim and Kim (2013)) were also designed to get the desired

segmentation results. Zhi and Shen (2018a) proposed a level set based method by incorporating saliency information and image intensity as region external energy to motivate the curve evolution. These models can handle the intensity inhomogeneity to some extent.

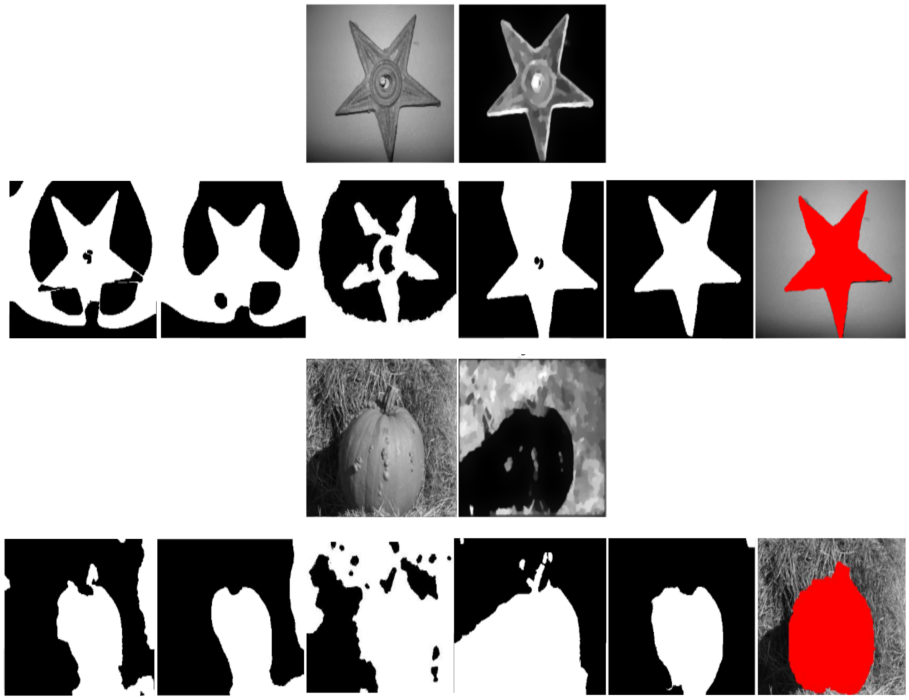

Fig. 11 Segmentation results on single-channel images. In the first and the third rows, the first column: images from the Alpert's dataset (size: 300×225); the second column: the corresponding intensity inhomogeneity images respectively. In the second and the fourth rows, from the first column to the last column: segmentation results of the methods in Cai et al (2017), Li et al (2010), Zhi and Shen (2018b), Wang et al (2009), Li et al (2020) and the ground truth.

In Li et al (2020), a new three-stage segmentation framework was proposed based on the SaT method and the intensity inhomogeneity information of an image. The first stage in this framework is to perform a dimension lifting method. An intensity inhomogeneity image is added as an additional channel, which results in a vector-valued image. In the second stage, a SaT model is applied to each channel of the vector-valued image to obtain a smooth approximation. The semi–proximal alternating direction method of multipliers (sPADMM) Han et al (2018) is used to solve this model and it is proved that the sPADMM for solving this convex model has

Q-linear convergence rate. In the last stage, a thresholding method is applied to the smoothed vector-valued image to get the final segmentation.

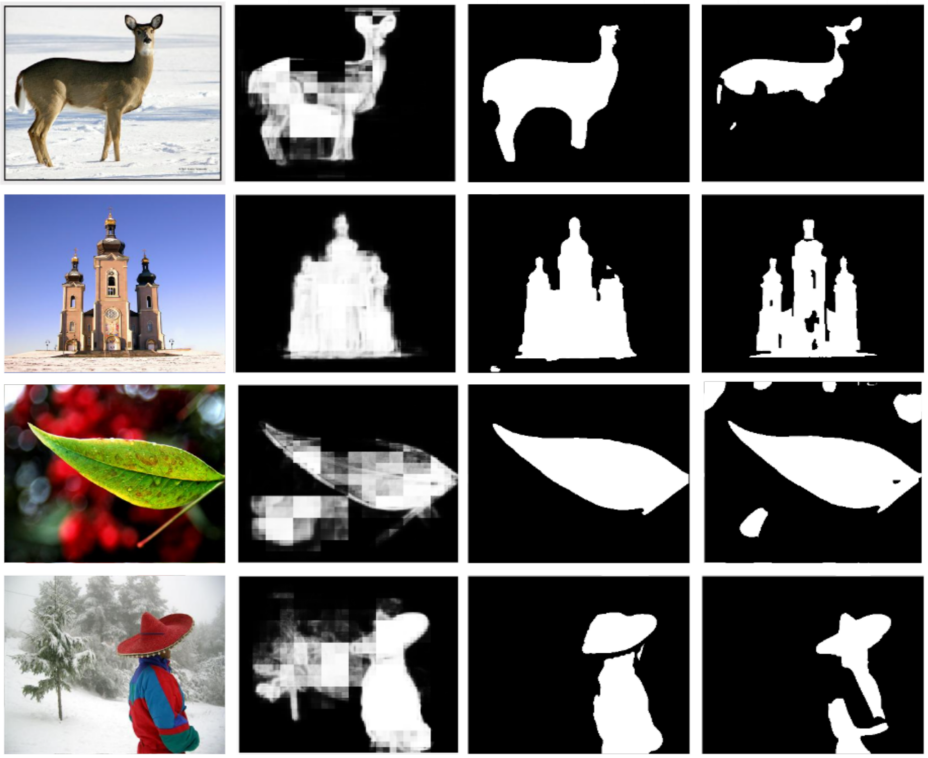

(a) given image (b) U-net (c) Li et al (2020) (d) Cai et al (2017)

Fig. 12 Column (a): The original images from the 100 test dataset; column (b): segmentation results of the U-net method Ronneberger et al (2015); column (c): segmentation results of the method in Li et al (2020); and column (d): segmentation results of the method in Cai et al (2017).

Figure 11 shows the great performance of the three-stage method Li et al (2020) incorporating intensity inhomogeneity information, and Figure 12 demonstrates that Li et al (2020) provides the most accurate segmentation results in comparison with five state-of-the-art methods including a deep learning approach (U-net method) Ronneberger et al (2015). More details please refer to Li et al (2020).

Conclusions

In this article, we introduced the the SaT (smoothing and thresholding) segmentation methodology, and methods developed based on this methodology with many applications in image processing. The SaT method provides an efficient and flexible methodology for image segmentations. It is easy to adapt the SaT method for various segmentation tasks. The SaT approach connects the segmentation problem to image restoration problem. Recent researches show that the SaT method can also be applied to classification problems. We hope that, with this article, the SaT method can reach audiences from broader areas and can inspire more cross disciplinary researches.

References

Ambrosio L, Tortorelli V (1990) Approximation of functions depending on jumps by elliptic functionals via t-convergence. Communications in Pure and Applied Mathematics 43:999–1036

Aubert G, Aujol J (2008) A variational approach to removing multiplicative noise. SIAM J Appl Math 68:925–946

Audet P (2014) Toward mapping the effective elastic thickness of planetary lithospheres from a spherical wavelet analysis of gravity and topography. Phys Earth Planet In 226:48–82

Baldi P, Kerkyacharian G, Marinucci D, Picard D (2009) Asymptotics for spherical needlets. Ann Stat 37(3):1150–1171

Bar L, Chan T, Chung G, Jung M, Kiryati N, Mohieddine R, Sochen N, Vese L (2011) Mumford and shah model and its applications to image segmentation and image restoration. In: Handbook of Mathematical Imaging, Springer, pp 1095–1157

Bauer B, Cai X, Peth S, Schladitz K, Steidl G (2017) Variational-based segmentation of biopores in tomographic images. Computers & Geosciences 98:1–8

Bellettini G, Paolini M, Verdi C (1991) Convex approximations of functionals with curvature. Mat Appl 2(4):297–306

Benninghoff H, Garcke H (2014) Efficient image segmentation and restoration using parametric curve evolution with junctions and topology changes. SIAM J Imaging Sci 7(3):1451–1483

Blake A, Zisserman A (1987) Visual Reconstruction. MIT Press, Cambridge, MA

Bresson X, Esedoglu S, Vandergheynst P, Thiran J, Osher S (2007) Fast global minimization of the active contour/snake model. Journal of Mathematical Imaging and Vision 28(2):151–167

Brown E, Chan T, Bresson X (2012) Completely convex formulation of the chan-vese image segmentation model. International Journal of Computer Vision 98:103–121

Brox T, Rousson M, Deriche R, Weickert J (2010) Colour, texture, and motion in level set based segmentation and tracking. Image Vision Comput 28:376–390

Cai J, Chan R, Shen Z (2008) A framelet-based image inpainting algorithm. Appl Comput Harmon Anal 24:131–149

Cai X (2015) Variational image segmentation model coupled with image restoration achievements. Pattern Recognition 48(6):2029–2042

Cai X, Steidl G (2013) Multiclass segmentation by iterated ROF thresholding. In: Energy Minimization Methods in Computer Vision and Pattern Recognition, Springer, pp 237–250

Cai X, Chan R, Morigi S, Sgallari F (2011) Framelet-based algorithm for segmentation of tubular structures. In: SSVM, Springer, p LNCS6667

Cai X, Chan R, Morigi S, Sgallari F (2013a) Vessel segmentation in medical imaging using a tight-frame based algorithm. SIAM Journal on Imaging Sciences 6(1):464–486

Cai X, Chan R, Zeng T (2013b) A two-stage image segmentation method using a convex variant of the Mumford–Shah model and thresholding. SIAM J Imaging Sci 6(1):368–390

Cai X, Fitschen J, Nikolova M, Steidl G, Storath M (2015) Disparity and optical flow partitioning using extended potts priors. Information and Inference: A Journal of the IMA 4:43–62

Cai X, Chan R, Nikolova M, Zeng T (2017) A three-stage approach for segmenting degraded color images: smoothing, lifting and thresholding (SLaT). J Sci Comput 72(3):1313–1332, DOI 10.1007/s10915-017-0402-2, URL https://doi.org/10.1007/s10915-017-0402-2

Cai X, Chan RH, Schönlieb CB, Steidl G, Zeng T (2019) Linkage between piecewise constant Mumford–Shah model and Rudin–Osher–Fatemi model and its virtue in image segmentation. SIAM Journal on Scientific Computing 41(6):B1310–B1340

Cai X, Wallis CGR, Chan JYH, McEwen JD (2020) Wavelet-based segmentation on the sphere. Pattern Recognition 100:https://doi.org/10.1016/j.patcog.2019.107,081

Candés E, Donoho D (2005) Continuous curvelet transform: Ii. discretization and frames. Appl Comput Harmon Anal 19(2):198–222

Cardelino J, Caselles V, Bertalmio M, Randall G (2013) A contrario selection of optimal partitions for image segmentation. SIAM J Imaging Sci 6(3):1274–1317

Chambolle A (2005) Total variation minimization and a class of binary MRF models. In: Rangarajan A, Vemuri BC, Yuille AL (eds) Energy Minimization Methods in Computer Vision and Pattern Recognition – EMMCVPR 2005, Lecture Notes in Computer Science, vol 3757, Springer, Berlin, pp 136–152

Chambolle A, Pock T (2011) A first-order primal-dual algorithm for convex problems with applications to imaging. Journal of Mathematical Imaging and Vision 40(1):120–145

Chambolle A, Caselles V, Novaga M, Cremers D, Pock T (2010) An introduction to total variation for image analysis. Theoretical Foundations and Numerical Methods for Sparse Recovery, Radon Ser Comput Appl Math 9:263–340

Chan J, Leistedt B, Kitching T, McEwen JD (2017) Second-generation curvelets on the sphere. IEEE Trans Sig Proc 65(1):5–14

Chan R, Yang H, Zeng T (2014) A two-stage image segmentation method for blurry images with poisson or multiplicative gamma noise. SIAM Journal on Imaging Sciences 7(1):98–127

Chan R, Yang H, Zeng T (2019) Total Variation and Tight Frame Image Segmentation with Intensity Inhomogeneity. arXiv e-prints p arXiv:1904.01760

Chan R, Kan KK, Nikolova M, Plemmons RJ (2020) A two-stage method for spectral-spatial classification of hyperspectral images. Journal of Mathematical Imaging and Vision 62:790–807

Chan TF, Vese LA (2001a) Active contours without edges. IEEE Transactions on Image Processing 10(2):266–277

Chan TF, Vese LA (2001b) Active contours without edges. IEEE Trans Image Process 10(2):266–277

Chan TF, Sandberg BY, Vese LA (2000) Active contours without edges for vector-valued images. Journal of Visual Communication and Image Representation 11(2):130–141

Chan TF, Esedoglu S, Nikolova M (2006a) Algorithms for finding global minimizers of image segmentation and denoising models. SIAM Journal on Applied Mathematics 66(5):1632–1648

Chan TF, Esedoglu S, Park F, Yip A (2006b) Total variation image restoration: Overview and recent developments. Springer-Verlag, New York, Handbook of Mathematical Models in Computer Vision, pp 17–31

Chapman B, Parker D, Stapelton J, Parker D (2004) Intracranial vessel segmentation from time-of-flight mra using pre-processing of the mip z-buffer: accuracy of the zbs algorithm. Medical Image Analysis 8(2):113–126

Chen J, Amini A (2004) Quantifying 3d vascular structures in mra images using hybrid pde and geometric deformable models. IEEE Trans on Medical Imaging 23(10):1251–1262

Cremers D, Rousson M, Deriche R (2007a) A review of statistical approaches to level set segmentation: integrating color, texture, motion and shape. International Journal of Computer Vision 72(2):195–215

Cremers D, Rousson M, Deriche R (2007b) A review of statistical approaches to level set segmentation: Integrating color, texture, motion, and shape. Int J Comput Vis 72(2):195–215

Datt B, McVicar T, Van Niel T, Jupp D, Pearlman J (2003) Preprocessing eo-1 hyperion hyperspectral data to support the application of agricultural indexes. IEEE Trans Geosci Remote Sens 41(6):1246–1259

Dong B, Chien A, Shen Z (2010) Frame based segmentation for medical images. Commun Math Sci 32:1724–1739

Dong B, Chien A, Shen Z (2011) Frame based segmentation for medical images. Commun Math Sci 9(2):551–559

Durand S, Fadili J, Nikolova M (2010) Multiplicative noise removal using l1 fidelity on frame coefficients. J Math Imaging Vis 38:201–226

Eismann M, Stocker A, Nasrabadi N (2009) Automated hyperspectral cueing for civilian search and rescue. Proc IEEE 97(6):1031–1055

Fauvel M, Tarabalka Y, Benediktsson J, Chanussot J, Tilton J (2013) Advances in spectral-spatial classification of hyperspectral images. Proc IEEE 101(3):652–675

Franchini E, Morigi S, Sgallari F (2009) Composed segmentation of tubular structures by an anisotropic pde model. In: X.-C. Tai et al. (eds.): SSVM 2009, LNCS5567, pp 75–86

Franchini E, Morigi S, Sgallari F (2010) Segmentation of 3d tubular structures by a pde-based anisotropic diffusion model. In: M. Dæhlen et al. (eds.): MMCS 2008, LNCS5862, pp 224–241

Ge Q, Liang X, Wang L, Zhang Z, Wei Z (2015) A hybrid active contour model with structured feature for image segmentation. Signal Process 108:147–158

Geman S, Geman D (1984) Stochastic relaxation, Gibbs distributions, and the Bayesian restoration of images. IEEE Transactions on Pattern Analysis and Machine Intelligence 6:721–741

Goldstein T, Osher S (2009) The split Bregman method for l1-regularized problems. SIAM Journal on Imaging Sciences 2(2):323–343

Gooya A, Liao H, et al (2008) A variational method for geometric regularization of vascular segmentation in medical images. IEEE Trans Image Process 17(8):1295–1312

Gowen A, O'Donnell C, Cullen P, Downey G, Frias J (2007) Hyperspectral imaging-an emerging process analytical tool for food quality and safety control. Trends Food Sci Technol 18(12):590–598

Han D, Sun D, Zhang L (2018) Linear rate convergence of the alternating direction method of multipliers for convex composite programming. Mathematics of Operations Research 43(2):622–637

He Y, Hussaini MY, Ma J, Shafei B, Steidl G (2012) A new fuzzy c-means method with total variation regularization for image segmentation of images with noisy and incomplete data. Pattern Recognition 45:3463–3471

Hörig B, Kühn F, Oschütz F, Lehmann F (2001) Hymap hyperspectral remote sensing to detect hydrocarbons. Int J Remote Sens 22(8):1413–1422

Jung YM, Kang SH, Shen J (2007) Multiphase image segmentation via Modica-Mortola phase transition. SIAM Journal on Applied Mathematics 67(5):1213–1232

Kay D, Tomasi A, et al (2009) Color image segmentation by the vector-valued Allen–Cahn phase-field model: a multigrid solution. Image Processing, IEEE Transactions on 18(10):2330–2339

Kim W, Kim C (2013) Active contours driven by the salient edge energy model. IEEE Trans Image Process 22:1667–1673

Kirbas C, Quek F (2004) A review of vessel extraction techniques and algorithms. CV Computing Surveys 36:81–121

Krissian K, Malandain G, Ayache N, Vaillant R, Trousset Y (2000) Model-based detection of tubular structures in 3d images. CVIU 80:130–171

Leistedt B, McEwen J, Vandergheynst P, Wiaux Y (2013) S2let: A code to perform fast wavelet analysis on the sphere. Astronomy & Astrophysics 558(A128):1–9

Lellmann J, Schnörr C (2011) Continuous multiclass labeling approaches and algorithms. SIAM Journal on Imaging Sciences 44(4):1049–1096

Li C, Kao C, Gore J, Ding Z (2008) Minimization of region-scalable fitting energy for image segmentation. IEEE Trans Image Process 17:1940–1949

Li F, Ng M, Zeng T, Shen C (2010) A multiphase image segmentation method based on fuzzy region competition. SIAM Journal on Imaging Sciences 3(2):277–299

Li S, Hai Y (2010) A full-view spherical image format. ICPR pp 2337–2340

Li X, Yang X, Zeng T (2020) A three-stage variational image segmentation framework incorporating intensity inhomogeneity information. SIAM Journal on Imaging Sciences 13(3):1692–1715

Lorigo L, Faugeras O, Grimson E, et al (2001) Curves: curve evolution for vessel segmentation. Medical Image Analysis 5:195–206

Manolakis D, Shaw G (2002) Detection algorithms for hyperspectral imaging applications. IEEE Signal Process Mag 19(1):29–43

Martin D, Fowlkes C, Tal D, Malik J (2001) A database of human segmented natural images and its application to evaluating segmentation algorithms and measuring ecological statistics. In: ICCV, vol 2, pp 416–423

McEwen J, Hobson M, Mortlock D, Lasenby A (2007a) Fast directional continuous spherical wavelet transform algorithms. IEEE Trans Signal Process 55(2):520–529

McEwen J, Vielva P, Wiaux Y, et al (2007b) Cosmological applications of a wavelet analysis on the sphere. J Fourier Anal and Appl 13(4):495–510

McEwen J, Durastanti C, Wiaux Y (2018) Localisation of directional scale-discretised wavelets on the sphere. Applied Comput Harm Anal 44(1):59–88

Michailovich O, Rathi Y (2010) On approximation of orientation distributions by means of spherical ridgelets. IEEE Trans Sig Proc 19(2):461–477

Mumford D, Shah J (1989) Optimal approximation by piecewise smooth functions and associated variational problems. Communications on Pure and Applied Mathematics XLII:577–685

Paschos G (2001) Perceptually uniform color spaces for color texture analysis: an empirical evaluation. Image Processing, IEEE Transactions on 10(6):932–937

Patel N, Patnaik C, Dutta S, Shekh A, Dave A (2001) Study of crop growth parameters using airborne imaging spectrometer data. Int J Remote Sens 22(12):2401–2411

Pock T, Chambolle A, Cremers D, Bischof H (2009a) A convex relaxation approach for computing minimal partitions. In: Computer Vision and Pattern Recognition, 2009. CVPR 2009. IEEE Conference on, IEEE, pp 810–817

Pock T, Cremers D, Bischof H, Chambolle A (2009b) An algorithm for minimizing the piecewise smooth mumford-shah functional. In: ICCV

Rathi Y, Michailovich O, Setsompop K, et al (2011) Sparse multi-shell diffusion imaging. MICCAI, International Conference on Medical Image Computing and Computer-Assisted Intervention 14(2):58–65

Ronneberger O, Fischer P, Brox T (2015) U-net: Convolutional networks for biomedical image segmentation. In: International Conference on Medical image computing and computer-assisted intervention, Springer, pp 234–241

Rotaru C, Graf T, Zhang J (2008) Color image segmentation in HSI space for automotive applications. Journal of Real-Time Image Processing 3(4):311–322

Rudin L, Osher S, Fatemi E (1992) Nonlinear total variation based noise removal algorithms. Physica D 60:259–268

Sandberg B, Kang S, Chan T (2010) Unsupervised multiphase segmentation: a phase balancing model. IEEE Transactions on Image Processing 19:119–130

Schmitt J, Starck J, Casandjian J, Fadili J, Grenier I (2012) Multichannel poisson denoising and deconvolution on the sphere: application to the fermi gamma-ray space telescope. Astronomy & Astrophysics 546(A114)

Shi J, Osher S (2008) A nonlinear inverse scale space method for a convex multiplicative noise model. SIAM J Imaging Sci 1:294–321

Simons F, Loris I, Nolet G, et al (2011) Solving or resolving global tomographic models with spherical wavelets, and the scale and sparsity of seismic heterogeneity. Geophys J Int 187:969–988

Starck J, Moudden Y, Abrial P, Nguyen M (2006) Wavelets, ridgelets and curvelets on the sphere. Astronomy & Astrophysics 446(3):1191–1204

Steidl G, Teuber T (2010) Removing multiplicative noise by Douglas-Rachford splitting methods. Journal of Mathematical Imaging and Vision 36(2):168–184

Stein D, Beaven S, Hoff L, Winter E, Schaum A, Stocker A (2002) Anomaly detection from hyperspectral imagery. IEEE Signal Process Mag 19(1):58–69

Storath M, Weinmann A (2014) Fast partitioning of vector-valued images. SIAM Journal on Imaging Sciences 7(3):1826–1852

Sum K, Cheung P (2008) Vessel extraction under non-uniform illumination: A level set approach. IEEE Trans Biomed Eng 55(1):358–360

T Le RC, Asaki TJ (2007) A variational approach to reconstructing images corrupted by poisson noise. J Math Imaging Vis 27:257–263

Vese L, Chan T (2002) A multiphase level set framework for image segmentation using the mumford and shah model. International Journal of Computer Vision 50(3):271–293

Wallis C, Wiaux Y, McEwen J (2017) Sparse image reconstruction on the sphere: analysis and synthesis. IEEE Trans Image Process 26(11):5176–5187

Wang L, Li C, Sun Q, Xia D, Kao CY (2009) Active contours driven by local and global intensity fitting energy with application to brain mr image segmentation. Computerized medical imaging and graphics 33(7):520–531

Wang X, Huang D, Xu H (2010) An efficient local chan-vese model for image segmentation. Pattern Recogn 43:603–618

Wang X, Tang Y, Masnou S, Chen L (2015) A global/local affinity graph for image segmentation. Image Processing, IEEE Transactions on 24(4):1399–1411

Yan P, Kassim A (2006) Mra image segmentation with capillary geodesic active contours. Medical Image Analysis 10:317–329

Yuan J, Bae E, Tai XC (2010a) A study on continuous max-flow and min-cut approaches. In: 2010 IEEE Computer Society Conference on Computer Vision and Pattern Recognition, IEEE, pp 2217–2224

Yuan J, Bae E, Tai XC, Boykov Y (2010b) A continuous max-flow approach to potts model. In: European Conference on Computer Vision, pp 379–392

Zach C, Gallup D, J-MFrahm, Niethammer M (2008) Fast global labeling for real-time stereo using multiple plane sweeps. Vision, Modeling, and Visualization Workshop

Zhang Y, Matuszewski B, Shark L, Moore C (2008) Medical image segmentation using new hybrid level-set method. In: 2008 Fifth International Conference BioMedical Visualization: Information Visualization in Medical and Biomedical Informatics, pp 71–76

Zhi X, Shen H (2018a) Saliency driven region-edge-based top down level set evolution reveals the asynchronous focus in image segmentation. Pattern Recogn 80:241–255

Zhi XH, Shen HB (2018b) Saliency driven region-edge-based top down level set evolution reveals the asynchronous focus in image segmentation. Pattern Recognition 80:241–255

Zonoobi D, Kassim A, Shen W (2009) Vasculature segmentation in mra images using gradient compensated geodesic active contours. J Sign Process Syst 54:171–181